G. Di Ilio, V. Krastev, F. Piscaglia, G. Bella
Hybrid URANS/LES Turbulence Modeling for Spray Simulation: a Computational Study
SAE TECHNICAL PAPER, 2019-01-0270, 2019, p. 1-16
doi:10.4271/2019-01-0270

19PFL-0444

Hybrid URANS/LES Turbulence Modeling for Spray Simulation: a Computational Study

G. Di Ilio, V. Krastev, G. Bella
University of Tor Vergata, Rome (Italy)

F. Piscaglia
Dept. of Aerospace Science and Technology, Politecnico di Milano (Italy)

Abstract

Turbulence modeling for fuel spray simulation plays a prominent role in the understanding of the flow behavior in Internal Combustion Engines (ICEs). Currently, a lot of research work is actively spent on Large Eddy Simulation (LES) turbulence modeling as a replacement option of standard Reynolds averaged approaches in the Eulerian-Lagrangian spray modeling framework, due to its capability to accurately describe flow-induced spray variability and to the lower dependence of the results on the specific turbulence model and/or modeling coefficients. The introduction of LES poses, however, additional questions related to the implementation/adaptation of spray-related turbulence sources and to the rise of conflicting numerics and grid requirements between the Lagrangian and Eulerian parts of the simulated flow. About the latter, an efficient alternative might be found in hybrid URANS/LES formulations, which are still relatively unexplored for spray modeling applications and for ICE modeling in general. In this work, we conduct a systematic analysis aimed to assess the effects of several URANS, LES and hybrid turbulence modeling formulations on the spray dynamics. The hybrid form is based on a purposely developed version of the k-g URANS closure, and the simulation campaign is focused on a standard n-dodecane evaporating spray case in a constant volume vessel configuration. The spray is modeled within the Eulerian-Lagrangian framework, with primary and secondary breakup taken into account by means of the Kelvin-Helmholtz-Rayleigh-Taylor (KHRT) model. Further, we investigate on the effects due to the Stochastic Turbulence Dispersion (STD) of parcels. Numerical experiments are carried out via the open-source CFD code OpenFOAM. The results are validated against the baseline experimental data for evaporating ECN Spray A and with previous computational findings available in literature.

Introduction

Automotive engine manufacturers are currently facing great technical challenges, due to the sharply increasing restrictions on polluting emissions and primary energy consumption that are being implemented in the European Union and other highly developed countries. Most of the modern small and medium-sized engines are based on direct fuel injection technologies, being either spark-ignited gasoline units or compression-ignited diesel units. Therefore, the development of high-fidelity simulation methods for fuel spray characterization is crucial, in order to help injector and engine designers to devise cleaner and more efficient thermal power units.

At present, multidimensional spray modeling in engines is commonly based on the Eulerian-Lagrangian approach, in which the gaseous phase is treated as a continuum while the liquid phase is described through a Lagrangian Particle Tracking (LPT) method. Spray-turbulence interaction is accounted for through a suitable turbulence modeling choice, which may belong either to the Unsteady Reynolds Averaged Navier-Stokes (URANS) or Large Eddy Simulation (LES) families. We recall here that the term URANS is referred to the time-dependent form of any standard RANS-based approach, where the averaged momentum and turbulent scalar transport equations are solved in time. Compared to URANS, which still relies on a statistical description of turbulence, LES allows to accurately reproduce local and instantaneous changes in the flow parameters, thus providing a better insight in the physical and chemical processes that are typical of Internal Combustion Engines (ICE) operation. Due to such features, LES has been extensively examined for ICE simulation in the past 20 years [1], making remarkable steps towards full maturity for industry-grade applications [2, 3]. In spite of this, the coupling of LPT with LES for spray description may still be considered as a rather new option [4–7], thus requiring further research efforts to better assess (and eventually improve) the spray-turbulence modeling integration. Broadly speaking, LES is well suited for the dilute spray region [6], where the typical LES grid resolution is supposed to match well the numerical requirements of LPT. On the other side, an excessively high mesh refinement may violate some of the hypotheses that lie behind the Lagrangian tracking concept. Additionally, special attention is needed to properly account for dispersion effects at a sub-grid level [1, 7], which may significantly influence the liquid phase mass distribution at certain spray

regimes [8].

Roughly from 2009 [9], hybrid URANS/LES methodologies are being investigated to complement LES in ICE applications. Since then, a number of approaches have been assessed, including the Scale-Adaptive Simulation (SAS) [10, 11], Very Large Eddy Simulation (VLES) methods [12, 13] and different flavors of the Detached Eddy Simulation (DES) [9, 10, 14–18] technique. Some of the reasons for considering hybrids methods for ICE simulation instead of conventional LES are the significant reduction of the overall computational costs, by enabling LES only where it is actually needed, and a simpler setup of the boundary conditions for high-Re flows at the walls and at the open ends [19]. Most of the above mentioned studies have shown promising results, but they were essentially limited to cold-flow engine analyses. To the best of the authors' current knowledge, there are no ICE-related published works on the coupling of hybrids with combustion or LPT spray sub-models, thus leaving large room for further investigations in that field.

In the present paper we propose a systematic computational analysis to assess the consistency of an intentionally developed hybrid URANS/LES formulation, coupled with LPT spray modeling. The hybrid form follows a zonal modeling concept [16–18, 20], which allows to split the computational domain in pure-URANS, pure-LES or DES zones, with the aim of maximizing the benefits of each mode of operation by taking into account the physics involved and the available computational resources. In this initial study, numerical experiments are carried out on a standard non-reacting evaporating spray case in order to assess the spray-turbulence interplay under various grid refinement scenarios. Along with the available experimental data sets [21], state-of-the-art URANS and LES simulations are performed for comparison. The remainder of the paper is organized as follows: first the hybrid turbulence modeling methodology is introduced; then, Lagrangian governing equations and spray sub-models used in this work are defined; afterwards, we describe the problem under consideration and we provide details on the numerical setup; finally, we present our findings along with a discussion on the results obtained for URANS, LES and DES analysis. In the conclusions, we summarize the main results achieved and we include considerations and suggestions for future possible extensions of the work.

Turbulence modeling

The hybrid turbulence modeling used in the present work is built on top of the DES principle, which can be generally applied to the unsteady form of a one- or two-equation RANS closure [22, 23]. The starting point is the so called k-g URANS model, where g represents the square root of a characteristic turbulent time scale, namely:

$$g = \sqrt{\frac{k}{\varepsilon}} = \sqrt{\frac{1}{\beta^* \omega}} \tag{1}$$

with β^*= 0.09. A transport equation for g was firstly derived in the work from Kalitzin et al. [24], where the relationship (1) was used to rearrange the ω-equation in the k-ω standard model [25]. Using a g-based formulation is mainly justified by the much smoother scaling compared to ω (or ε). This is especially true close to solid walls, where the following scaling laws apply:

$$\omega \propto \frac{1}{y^2} \Longrightarrow g \propto y \tag{2}$$

with y being the wall-normal coordinate. In previous works [26, 27], we developed a modified k-g closure by introducing a realizability constraint on the characteristic turbulent time scale [28, 29]. In this new form, the model transport equations are:

$$\rho \frac{\partial k}{\partial t} + \nabla \cdot (\rho \mathbf{U} k) = \mathcal{P} - \mathcal{S}_k + \nabla \cdot \left[\left(\frac{\mu_t}{\sigma_k} + \mu \right) \nabla k \right] \tag{3}$$

$$\begin{aligned} \rho \frac{\partial g}{\partial t} + \nabla \cdot (\rho \mathbf{U} g) =& \rho \frac{\beta g}{2\beta^* \tau} - \frac{\alpha g^3}{2k\tau} \mathcal{P} + \nabla \cdot \left[\left(\frac{\mu_t}{\sigma_g} + \mu \right) \nabla g \right] + \\ &+ \left(\frac{\mu_t}{\sigma_g} + \mu \right) \frac{3g}{\tau} (\nabla g \cdot \nabla g) \end{aligned} \tag{4}$$

where ρ is the fluid density, $\mathcal{P}$ is the standard turbulence production term and α, β, σ_g, σ_k are the remaining closure constants of the original k-g form. The turbulent viscosity μ_t is given by:

$$\mu_t = \rho \beta^* k \tau \tag{5}$$

with the turbulent time scale τ being evaluated according to [27–29]:

$$\tau = \min \left(g^2,\ a_\tau \tau_{lim} \right) \tag{6}$$

where:

$$\tau_{lim} = \frac{2}{3\beta^*} \sqrt{\frac{3}{8|\mathbf{E}|^2}} \tag{7}$$

with $|\mathbf{E}|^2$ = magnitude squared of the mean rate-of-strain tensor and $a_\tau \leq 1$ being a model constant. In [29] it is stated that a_τ should not go below 0.6, in order to avoid an erroneous limiter activation in free-shear layers. Therefore, the recommended value range for a_τ is $0.6 \leq a_\tau \leq 1$.

A two-equation DES model can be subsequently obtained by modifying the turbulent kinetic energy sink term $\mathcal{S}_k$ as follows [23]:

$$\mathcal{S}_{k,RANS} = \rho \frac{k}{\tau} = \rho \frac{k^{3/2}}{l_{RANS}} \tag{8}$$

$$l_{RANS} = k^{1/2} \tau \tag{9}$$

$$\mathcal{S}_{k,DES} = F_{DES}\mathcal{S}_{k,RANS} \tag{10}$$

$$F_{DES} = \max\left(\frac{l_{RANS}}{C_{DES}\Delta},\ 1\right) \tag{11}$$

with Δ = local grid spacing parameter and $C_{DES} \approx O(1)$. Based on previous calibration tests [16], in the present work the C_{DES} value is set to 0.5. When the $C_{DES}\Delta$ term is smaller than the modeled length scale, F_{DES} reduces the turbulent viscosity and the model produces the canonical $\propto \Delta^{4/3}$ viscosity scaling in the inertial subrange of a homogeneous and isotropic turbulent energy spectrum [23]. Otherwise, the effect of F_{DES} vanishes ($F_{DES} = 1$) and the model reverts back to the original URANS formulation. This is also known as *seamless* DES [30], as the URANS-to-LES switching is automatically managed by the model itself, depending on the local flow and grid resolution conditions.

A natural extension of seamless DES is represented by zonal-DES (ZDES) [31–33], in which different parts of the computational domain are marked *a-priori* by the user as URANS, LES or DES. A straightforward zonal rearrangement of the F_{DES} function consists of:

$$F^*_{DES} = C_{z1}F_{DES} + (1 - C_{z1})\,F_{ZDES} \tag{12}$$

$$F_{ZDES} = C_{z2} + (1 - C_{z2})\left(\frac{l_{RANS}}{C_{DES}\Delta}\right) \tag{13}$$

where C_{z1} and C_{z2} are boolean switching parameters which might be alternatively equal to 0 or 1. Table 1 shows all the possible modes of operation produced by F^*_{DES}, depending on the different C_{z1} and C_{z2} combinations.

Table 1: Modes of operation determined by the C_{z1} and C_{z2} values.

C_{z1}	C_{z2}	*Simulation type*	*Mode*
0	1	URANS	I
0	0	LES	II
1	1/0	DES	III

Such zonal treatment follows the original ZDES framework [31], with no special turbulence coupling procedure implemented at the URANS/LES or URANS/DES interfaces. Nonetheless, since transport equations are kept the same in all zones, continuity of the transported turbulent scalars from one zone to another is automatically ensured.

In order to comprehensively evaluate the three modes of the k-g ZDES formulation, we include in the present work additional state-of-the art URANS and LES predictions. URANS simulations are performed with standard, realizable, and RNG k-ε closures [34–36], while LES results are obtained with the Smagorinksy [37] and WALE [38] models.

Liquid phase governing equations and spray sub-models

The LPT approach consists of describing the spray liquid phase as an ensemble of discrete droplets. All of the droplets having identical properties are combined into single parcels, which are tracked in a Lagrangian framework within the Eulerian gas phase. The employment of parcels rather then droplets allows a significant reduction of the computational cost, since the actual number of droplets in real sprays may be massively large.

The motion of parcels is described by the following set of Lagrangian equations:

$$\frac{d\mathbf{x}_p}{dt} = \mathbf{u}_p \tag{14}$$

$$\frac{d\mathbf{u}_p}{dt} = \frac{\mathbf{F}}{m_p} \tag{15}$$

where $\mathbf{x}_p$ and $\mathbf{u}_p$ are the parcel position and velocity, respectively, while $\mathbf{F}$ represents the drag force acting on the parcel. Each parcel is considered to have a spherical shape, and it is characterized by diameter d_p, density ρ_l and mass m_p. The drag force can be then expressed in terms of the drag coefficient C_D, as follows:

$$\mathbf{F} = \frac{1}{2}\rho_g A C_D |\mathbf{U}_{rel}|\mathbf{U}_{rel} \tag{16}$$

where A is the projected area, $|\mathbf{U}_{rel}|$ is the magnitude of the relative velocity $\mathbf{U}_{rel}$ between the parcel and the surrounding gas, and ρ_g is the gas phase density. The drag coefficient C_D is given by the following expression:

$$C_D = \begin{cases} \frac{24}{Re_p}\left(1 + \frac{Re_p^{2/3}}{6}\right) & Re_p < 1000 \\ 0.424 & Re_p \geq 1000 \end{cases} \tag{17}$$

where

$$Re_p = \frac{\rho_g |\mathbf{U}_{rel}| d_p}{\mu_g} \tag{18}$$

is defined as the parcel Reynolds number, with μ_g being the gas phase dynamic viscosity. By introducing the parcel characteristic time, as:

$$\tau_p = \frac{\rho_l d_p^2}{18\mu_g} \tag{19}$$

and using equations (16) and (18), the parcel momentum equation (15) can be written as follows:

$$\frac{d\mathbf{u}_p}{dt} = \frac{C_D Re_p \mathbf{U}_{rel}}{24\tau_p} \tag{20}$$

Stochastic Turbulent Dispersion

In general, the relative velocity between the liquid parcel and the surrounding gas phase can be expressed as follows:

$$\mathbf{U}_{rel} = \mathbf{u} + \mathbf{u}' - \mathbf{u}_p \tag{21}$$

where $\mathbf{u}$ is the gas phase velocity at the parcel position, $\mathbf{u}_p$ is the parcel velocity, while $\mathbf{u}'$ is a fluctuating component, namely a stochastic velocity, which accounts for turbulent

dispersion of parcels due to interaction with surrounding gas. Therefore, in order to solve the Lagrangian system of equations (14) and (20), a closure model for $\mathbf{u}'$ and, ultimately, for the instantaneous relative velocity $\mathbf{U}_{rel}$, is required.

In this work, we use the model by O'Rourke [39, 40]: the stochastic dispersion velocity component $\mathbf{u}'$ is sampled from a Gaussian distribution with zero mean and standard deviation equal to $\sigma = \sqrt{2k/3}$. Such a velocity is kept constant over a certain time interval, that is the so called turbulence correlation time, which is taken to be the minimum of an eddy transverse time t_R and an eddy life time t_E. In our study, we use $t_E = k/\varepsilon$ and $t_R = C_{ps}\left(k^{3/2}/\varepsilon\right)/|\mathbf{U}_{rel}|$, where $C_{ps} = 0.16432$. Once the turbulence correlation time is reached, a new value for $\mathbf{u}'$ is sampled.

In the current work, we study the effect of STD by using the model described above. Cases where STD modeling is not considered correspond to the condition $\mathbf{u}' = 0$.

Injection model

In the present work, the *blob* model [41] is used to model the injection of liquid phase. Among the others, the *blob* injection is one of the most simple and widely employed approaches in literature, and for this reason was chosen for this study. According to this model, the parcels are injected into the computational domain with uniform size, and with a uniform spatial velocity profile, which magnitude depends on the mass flow rate. In particular, we set the diameter characterizing each injected parcel equal to the one of the injector nozzle. The direction along which the parcels are injected is chosen to be a random angle within the spray cone. Following experimental measurements presented at first ECN workshop [42], we set the cone angle equal to $22°$.

Breakup model

The hybrid Kelvin-Helmholtz Rayleigh-Taylor (KHRT) model [41, 43, 44] in conjunction with the liquid breakup length theory [45] is used to simulate droplet breakup. This approach combines the KH model for the modeling of primary breakup with the RT instability theory for secondary breakup. In this Section, we briefly recall the main concepts of the model.

In the Kelvin-Helmholtz (KH) breakup model, the velocity difference across the interface between the liquid jet and the surrounding gas phase causes small perturbations, leading to a surface instability which amplifies until the formation and separation of droplets. If Λ_{KH} is the wavelength corresponding to the KH wave with maximum growth rate, a parent droplet breakups to form new droplets with radius r_c, such that:

$$r_c = B_0 \Lambda_{KH} \tag{22}$$

In equation (22), B_0 is a fixed constant, which is equal to 0.61. During breakup, the parent droplet loses mass. The rate of change of its radius depends from the equilibrium radius r_c of the child droplets as follows:

$$\frac{dr}{dt} = \frac{r - r_c}{\tau_{KH}} \tag{23}$$

with the characteristic time for the KH breakup τ_{KH} being defined as:

$$\tau_{KH} = \frac{3.788 B_1 r}{\Omega_{KH}\Lambda_{KH}} \tag{24}$$

where r denotes the radius of the initial droplet, Ω_{KH} is the frequency of the fastest growing wave and B_1 is an adjustable constant. As it will be discussed later, the breakup model constant B_1 has a significant impact on the spray modeling, since it controls the diameter reduction of secondary droplets. Overrated values for B_1 may lead to a reduction of breakup phenomena and increased liquid penetration. On the contrary, too low B_1 values may result in higher diameter reduction rate, thus leading to increased spray disintegration and reduced liquid penetration.
After the breakup, a parcel division process and a droplets regrouping take place. During this stage, liquid mass conservation and conservation of the Sauter Mean Radius (SMR) must be ensured. To account for this, we employ the procedure developed by Patterson and Reitz [44] that, for the sake of clarity, we recall here. By definition, the droplet SMR is given by:

$$r = 3\frac{V_p}{A_p} \tag{25}$$

where $V_p = 4/3\pi r^3 n$ and $A_p = 4\pi r^2 n$ are volume and area of the parcel, with n being the number of droplets within the parcel. According to [44], each *parent* parcel breakups giving rise to a *new parent* parcel, in which the larger droplets are grouped, and a *child* parcel, which is constituted by an ensemble of the smaller droplets. The mass balance can be written as follows:

$$\rho_l \frac{4}{3}\pi n r^3 = \rho_l \frac{4}{3}\pi n_{np} r_{np}^3 + \rho_l \frac{4}{3}\pi n_c r_c^3 \tag{26}$$

In equation 26, n and r are the number and the radius of droplets in the initial *parent* parcel, while subscripts *np* and *c* refer to the bigger droplets in the *new parent* parcel and the smaller droplets in the *child* parcel, respectively. Application of definition 25 leads to the conservation equation for the SMR, that is:

$$r = \frac{n_{np} r_{np}^3 + n_c r_c^3}{n_{np} r_{np}^2 + n_c r_c^2} \tag{27}$$

Combining the two relations 26 and 27, we obtain the following equation:

$$n r^2 = n_{np} r_{np}^2 + n_c r_c^2 \tag{28}$$

The radius of the smaller droplets r_c is given by equation 22, while the radius r for the *parent* parcel droplets comes from the solution of equation 23. Moreover, the number of bigger droplets in the *new parent* parcel n_{np} is assumed to be equal to the number of *parent* droplets at the beginning of the breakup process, namely n. Therefore, the two unknowns of equation 28 are the radius r_{np} and the number of droplets n_c. The former is found by solving the following cubic equation:

$$n r^2 (r - r_c) - n_{np} r_{np}^2 (r_{np} - r_c) = 0 \tag{29}$$

which is obtained after manipulation of equation 28 with 26. Afterwards, once the value of r_{np} is known, the latter is found by solving equation 26 for n_c, that is:

$$n_c = \frac{nr^3 - n_{np}r_{np}^3}{r_c^3} \tag{30}$$

The mass shed from the initial *parent* parcel can be therefore computed. Finally, the number of droplets n_{np} is updated by considering the mass of the *new parent* parcel, which is given by the difference between the mass of initial *parent* parcel and the shed mass, and the mass of droplets with radius r_{np}.
The KH mechanism so far described is used to predict the spray primary breakup.

The Rayleigh-Taylor (RT) model accounts for instability of the liquid-gas interfaces due to different densities of the fluids. In the present KHRT hybrid approach, the RT model is used to predict the secondary break-up of the droplets. According to this model, instabilities on the surface of the liquid drop are assumed to be growing if the wavelength Λ_{RT} corresponding to the fastest wave growth rate is smaller than the droplet diameter. The droplet breakup occurs once a characteristic breakup time is reached. This is defined as:

$$\tau_{RT} = \frac{C_\tau}{\Omega_{RT}} \tag{31}$$

where Ω_{RT} is the frequency of the fastest growing wave and C_τ is a correction factor, which is usually taken equal to 1. The diameter of the new droplets is then set equal to Λ_{RT}, thus:

$$r_c = \frac{\pi C_{RT}}{K_{RT}} \tag{32}$$

where K_{RT} is the wave number corresponding to the fastest growing wave.

As mentioned before, we embed the concept of liquid breakup length [43] within the KHRT model. According to this theory, the liquid within the intact liquid core is unlikely to be influenced by the RT instability. Therefore, only droplets beyond such a liquid core are assumed to be influenced by the RT breakup. The corresponding characteristic breakup length is defined as follows:

$$L_b = C_b d_n \sqrt{\frac{\rho_l}{\rho_g}} \tag{33}$$

where d_n is the nozzle diameter, C_b is an adjustable constant, while ρ_l and ρ_g are the liquid and gas phase densities, respectively. We track the position of each parcel during time. Then, RT instability is activated only for those parcels which distance from the injector is greater than the breakup length.

Other spray sub-models

We use the Ranz-Marshall correlation to evaluate the heat transfer between liquid phase and surrounding gas phase. As evaporation model we adopt the one formulated by Spalding [46], while boiling is modeled on the basis of the work of Zuo et al. [47]. Finally, no collision model was taken into consideration since it is widely accepted that, for evaporating sprays, collision of droplets has a minor influence.

Problem statement and numerical setup

Engine Combustion Network (ECN) [21] provides a comprehensive experimental database for sprays at various ambient, fuel type and injection conditions. In the present work, we carry out numerical simulations for the ECN non-reacting "`Spray A`" operating conditions. This case refers to the injection of n-dodecane ($C_{12}H_{26}$), which is a diesel fuel surrogate, in a constant volume vessel of cubic shape. Modeling the spray physics in a rather simple geometry enables us to validate the proposed numerical approach and understand its features while avoiding those uncertainties which are inherently related to the complex configuration of a real engine geometry.
For the "`Spray A`" case, the ambient gas prior to the start of injection is at 900 K and 6.0 MPa, while having a density of 22.8 kg/m^3. Its initial composition is given by the following volumetric concentration: 0% O_2, 6.52% CO_2, 3.77% H_2O, 89.71% N_2. The fuel is injected from a single hole, along the axial direction, during a time of 1.5 ms, at injection pressure and temperature of 150 MPa and 363 K, respectively. The injector nozzle diameter is 90 μm and the discharge coefficient is 0.89. An accurate representation of the injection rate profile can be crucial to properly reproduce the initial transient of the spray evolution. Therefore, for the numerical experiments, it is convenient to use a suitable fuel mass flow rate profile as inflow condition at the nozzle. The rate of injection (ROI) used in this work is generated by applying the CMT utility for "`Spray A`" modeling [48], which requires as an input the following parameters: discharge coefficient, fuel density, nozzle diameter, injection time, back and injection pressure. By setting these values to those corresponding to the "`Spray A`" configuration and operating conditions as given above, we obtain the ROI depicted in Figure 1, which is the one adopted in all of the simulations performed in the current study. The corresponding total injected mass is 3.56 mg. Input parameters for "`Spray A`" are summarized also in Table 2.

Table 2: Input parameters for "`Spray A`" operating conditions.

Fuel type	n-dodecane ($C_{12}H_{26}$)
Ambient composition (by volume)	0% O_2 6.52% CO_2 3.77% H_2O 89.71% N_2
Ambient gas temperature	900 K
Ambient gas pressure	6.0 MPa
Ambient gas density	22.8 kg/m^3
Injection duration	1.5
Injection mass	3.56 mg
Injection pressure	150 MPa
Injection temperature	363 K
Discharge coefficient	0.89
Injector nozzle diameter	90 μm

The computational domain geometry used in this work is a cube whose side has a length of 108 mm, thus resembling the constant volume vessel configuration adopted at

Sandia National Laboratory (SNL) for obtaining the experimental data.

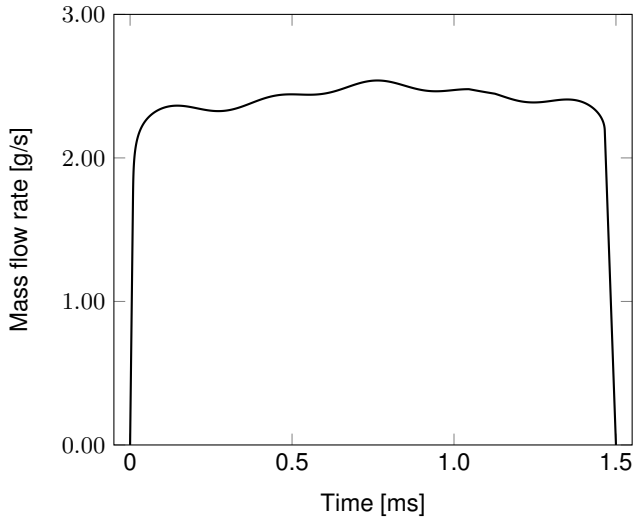

Figure 1: Rate of injection used as inflow condition.

The nozzle is located at the center of the top side of the domain, with the spray evolving along the perpendicular direction to this plane. Basing upon previous numerical studies on "`Spray A`" presented at the first ECN workshop [42], in all simulations, unless otherwise stated, we set initial uniform fields for either turbulence kinetic energy and turbulence dissipation rate with values equal to 0.735 m^2/s^2 and 5.67 m^2/s^3, respectively. Velocity fields are initialized to zero everywhere in the domain, for all of the turbulence modes analyzed. Moreover, we select a turbulent Schmidt number equal to 0.7, while the total number of injected parcels is 15000. The simulations are carried out using the finite volume open source code OpenFOAM-6 [49], that has been extended by a set of dynamic libraries, developed by the authors, to support hybrid turbulence modeling. A compressible flow solver, which makes use of a Pressure Implicit with Splitting Operators (PISO) algorithm, has been applied for the simulations. For URANS simulations, momentum convection is solved by means of a linear upwind differencing scheme, while for LES and hybrid simulations performed on mesh labelled as *m2* we use a linear scheme. A LUST scheme (blended 75% linear and 25% linear upwind) was instead preferred for LES simulations on mesh labelled as *m3*, to improve stability. For all cases, we adopt a linear upwind scheme also for transport of turbulent quantities, such as k, g and ε. Moreover, boundedness and stability of the numerical solution was improved by employing a flux limiter scheme for the discretization of gradient terms in turbulent quantities equations, in all of the cases and, also, for those in the momentum equation in URANS simulations. As far as time derivative discretization is concerned, we make use of a second order implicit Crank Nicolson scheme, with off-centering coefficient equal to 0.5, in all of the cases analyzed. For all cases, we employ a 3D Cartesian grid. In particular, we define a fully hexahedral uniform base mesh that is then refined by a cell-splitting approach. We skip details on the specific wall model adopted in the simulations, since for the "`Spray A`" case the vessel walls are located at a sufficient distance from the nozzle position to play no actual role in the spray flow evolution.

A case tuning procedure is initially carried out in order to identify the adjustable breakup model constant B_1 and validate the numerical setup. Among the others, B_1 is known to be the most influential spray model constant, therefore particular care must be taken to tune its value for the specific case under consideration. Inappropriate choice of this constant can lead to unrealistic prediction of the liquid phase behavior. By following [44] we varied B_1 within the range 1.73 - 60. We conduct such a preliminary analysis by performing URANS simulations with RNG k-ε closure, since this is currently the most widely used model in ICE numerical studies. This procedure is also used to determine proper simulation parameters, such as time-step, and optimal grid sizing configuration, which we use for the whole set of URANS simulations. We emphasize that, in general, given a set of spray model parameters, the simulation results are not grid independent. This is well documented in literature, and an insightful discussion is available in first ECN workshop Proceedings [42]. Several numerical studies have led to the conclusion that both liquid and vapor penetrations might be significantly affected by the mesh resolution. To a certain degree, it was also observed that time-step size might have not negligible effects on the numerical results. Despite this, mesh dependency is mainly related to the minimum grid spacing rather than the overall mesh configuration. This partially reduces the undesired effects related to the mesh dependency, thus allowing us to pose our analysis on a solid base. In fact, we remark that the aim of the present investigation is to compare different turbulence modeling strategies and, in particular, to understand the numerical behavior of an ad-hoc hybrid URANS/LES formulation, when the same set of spray model constants is kept. Results from the tuning procedure indicate that the best matching with experimental data by SNL for the "`Spray A`" case is achieved for $B_1 = 18$. Therefore, we select this value for all of the simulations performed in this study. Consistently with [43], we choose C_b equal to $B_1/2$. The overall set of KHRT breakup model constants is reported in Table 3.

Table 3: KHRT breakup model constants.

B_0	B_1	C_τ	C_{RT}	C_b
0.61	18	1	0.1	9

The final mesh accounts for about 600K cubic cells and it is constructed in such a way to be progressively finer towards the injector hole, namely in that region of the domain where the highest velocity gradients occur and the Lagrangian field of parcel is injected in the flow. The local refinements are realized by means of a sequentially cell-splitting strategy within coaxial cylindrical regions, whose axis is perpendicu-

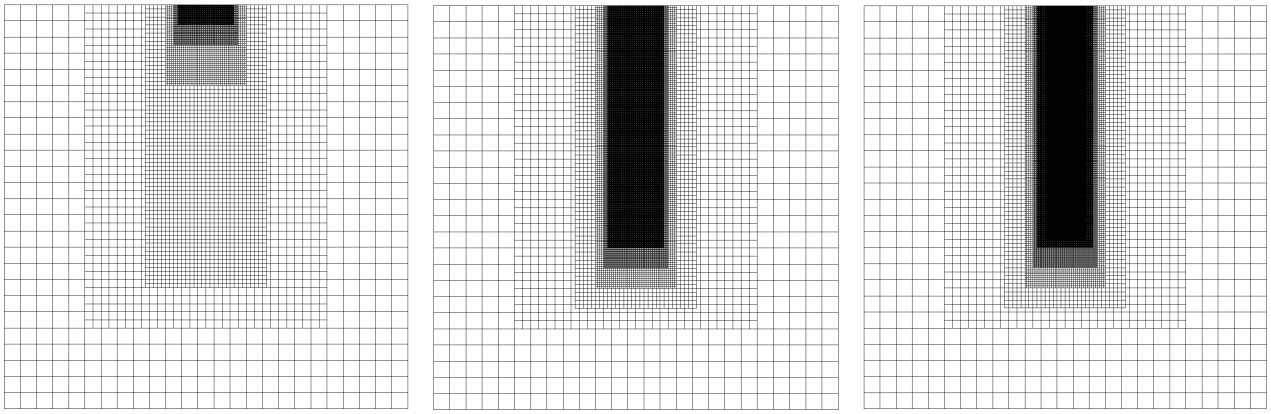

Figure 2: 2D cut-plane of the computational grids used in the paper; a) mesh *m1*, used for URANS simulations; b) mesh *m2*, used for LES and DES simulations; c) mesh *m3* used for LES simulations.

lar to the injector hole section at its center. The overall grid size ranges between 0.125 mm and 4 mm. A two dimensional cut-plane of the mesh is shown in Figure 2, while details for the cylindrical refinement regions are summarized in Table 4, where the radius and the height with respect to the injector nozzle location are provided. We shall refer to the described mesh as *m1* in the remaining part of the paper. We emphasize that a mesh with minimum grid spacing of 0.25 mm was found to be adequate to properly capture the main features of the analyzed spray in our URANS simulations. However, we observed an improvement of the slope of both vapor and liquid penetration, especially in the initial transient state, when a finer region with size of 0.125 mm is introduced in the close proximity of the injector hole.

Resolution of mesh *m1* cannot be sufficient to properly capture the spray dynamics when using a LES approach. Therefore, in such a case, a finer mesh must be used. To this aim, we construct two additional meshes, where the spray region is entirely discretized at a uniform resolution of 0.125 mm and 0.0625 mm, accounting roughly for 5 millions and 21 millions of cells, respectively. An illustration of the two meshes is provided in Figure 2. We shall refer to the described mesh as *m2* and *m3* in the text. Further details on each refinement level for both of the used mesh is provided in Table 4. Finally, we select a time-step equal to $2 \cdot 10^{-7}$ for all of the simulations performed on mesh *m1* and *m2*, while for cases on mesh *m3* we set $dt = 5 \cdot 10^{-8}$. We found these values to represent the best compromise, considering accuracy, stability and computational cost aspects.

Results and discussion

In this Section, we present numerical results for the three modes as introduced in Table 1. The results are provided in terms of liquid and vapor penetrations, mixture fraction and velocity profiles, given the availability of experimental data for these quantities. In particular, for LES and DES simulations, only one single realization for each case is simulated, and the results are then compared to the experimental mean together with the provided experimental dispersion. The liquid spray penetration is defined as the maximum distance from the injector nozzle to the farthest axial position where 95% of the liquid mass is found, while the vapor spray penetration is defined as the maximum distance from the injector nozzle to where the fuel mass fraction is 0.1%. Velocity, fuel mass fraction and viscosity fields are also presented and analyzed for a better understanding of the occurring flow phenomena.

URANS simulations analysis (mode I)

As described in previous Section, we use the RNG k-ε closure model to perform a case tuning study and validate the numerical setup. In Figure 3 we compare the obtained liquid and vapor penetration trends with those from different turbulence models, namely standard and realizable k-ε. All the simulations were performed on mesh *m1*. The results are plotted against experimental data from SNL.

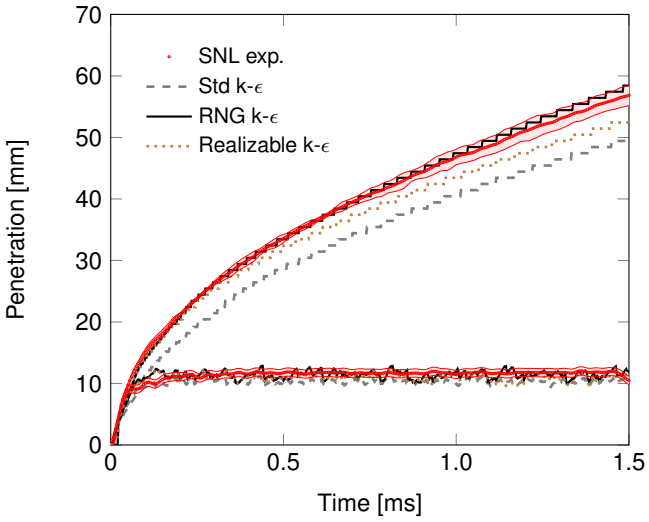

Figure 3: Effects of URANS turbulence model on liquid and vapor penetration. Results are compared with experimental data of SNL [21]. The filled area corresponds to the experimental standard deviation.

We notice that the effect of URANS turbulence models on liquid penetration is not pronounced. All of the considered

Table 4: Detailed description of refinement regions for all meshes: *m1*,*m2* and *m3*.

Refinement level	Size [mm]	Radius [mm]			Height [mm]		
		$m1$	$m2$	$m3$	$m1$	$m2$	$m3$
1	2.0000	30	30	30	80	80	80
2	1.0000	15	15	15	70	75	75
3	0.5000	10	10	10	20	70	70
4	0.2500	8	8	8	10	65	65
5	0.1250	7	7	7	5	60	60
6	0.0625	\	\	5	\	\	58

approaches match the experimental data very well. Conversely, there is a significant discrepancy among the vapor penetration predictions over time. The result obtained with RNG k-ε model is in good agreement with experimental measurements, while the vapor penetration predicted by the other two models appears underestimated, especially for the standard k-ε case. These findings are in line with results from the first ECN workshop [42].

Following what stated in [29], a parametric study is conducted for the k-g closure strategy where the model constant a_τ is varied between 0.6 and 1.0. We underline here that the use of the k-g model for spray simulation is, to date, still unexplored. For this reason, a tuning procedure is required in order to establish a suitable value for a_τ. Numerical tests are carried out on mesh *m1*, with same numerical setup as for previously presented URANS cases. Figure 4 shows the results, in terms of liquid and vapor penetrations, obtained via URANS simulations with k-g closure model, for three different values of the parameter a_τ.

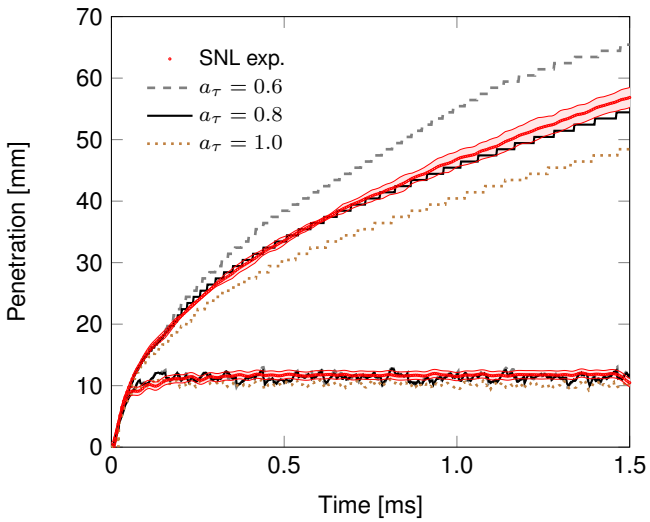

Figure 4: Effects of constant a_τ for URANS k-g model on liquid and vapor penetration. Results are compared with experimental data of SNL [21]. The filled area corresponds to the experimental standard deviation.

Although there are no substantial differences in estimation of liquid penetration, we found the effect of the model constant a_τ having a significant impact on the vapor penetration trend. Predictions of the initial transient state are in agreement to each others up to a time of roughly 0.1 ms. However, beyond this value, the slope of vapor penetration exhibits a growing trend with the increasing of a_τ. This leads to a significant overestimation of the final vapor tip for $a_\tau = 1$ and to an underestimation for the case $a_\tau = 0.6$. We found the optimal value to be $a_\tau = 0.8$, for which both liquid and vapor penetrations approaches closely the experimental data.

The initialization of the turbulence kinetic energy k field may affect significantly the simulation results. Therefore, we study the impact of such a condition by varying the initial value of the uniform field of k between 0.0735 m^2/s^2 and 7.35 m^2/s^2. Tests are carried out for the k-g closure model, with model constant a_τ equal to 0.8. The results are shown in Figure 5.

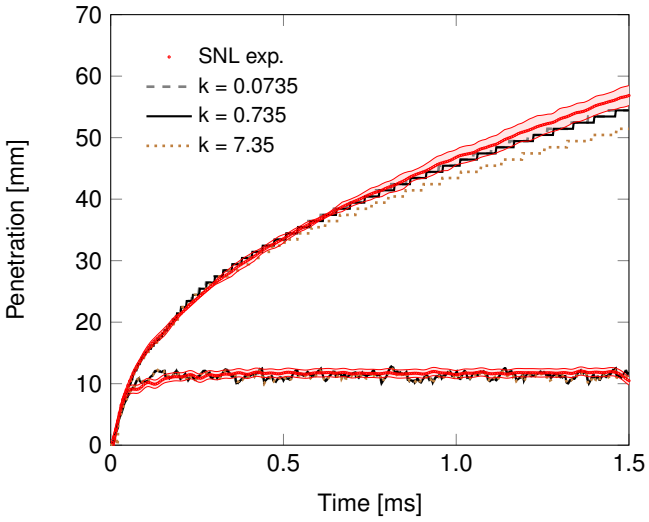

Figure 5: Effect of turbulence kinetic energy initialization for URANS k-g model (with a_τ = 0.8) on liquid and vapor penetration. Results are compared with experimental data of SNL [21]. The filled area corresponds to the experimental standard deviation.

We observe no significant dependency of results on the initial conditions when k is set from 0.735 m^2/s^2 to lower values. However, for k=7.35 m^2/s^2 the vapor tip is slightly under predicted. Liquid penetration is however never affected by the choice of the initial field of turbulent kinetic energy.

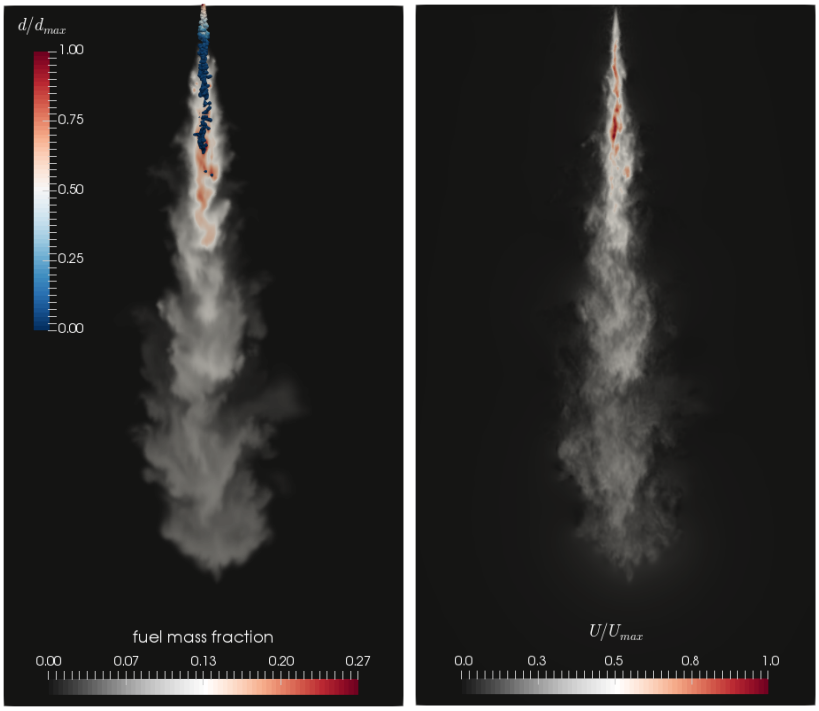

Figure 6: Instantaneous fuel mass fraction field (left) and velocity field (right) at 1.5 ms after the start of injection, for LES with k-g closure model (a_τ = 0.8) on mesh *m2*. Lagrangian field and velocity field are normalized to their maximum values, respectively.

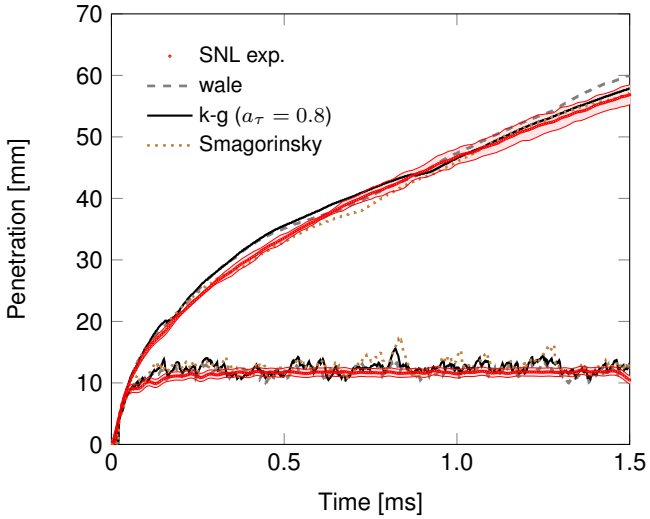

Figure 7: Effects of LES turbulence model on liquid and vapor penetration. Simulations are performed on mesh *m2* (minimum size: 0.125 mm). Results are compared with experimental data of SNL [21]. The filled area corresponds to the experimental standard deviation.

LES simulations analysis (mode II)

LES presented in this Section were performed on mesh *m2* and *m3*. Numerical setup and initial conditions are the same as those used for URANS simulations, except for the numerical scheme employed to solve the momentum convection, as already mentioned. Moreover, we set the value for the k-g model constant a_τ equal to 0.8 and we compare the obtained results with experimental data as well as with those from other well established model, such as WALE and Smagorinsky. In Figure 7 we show vapor and liquid penetrations predicted by the three models by simulations on mesh *m2*. All of the turbulent models provide very accurate results, which are in good agreement with experimental data. This finding confirms that the used mesh is suitable to be used for LES analysis and that a mesh resolution of 0.125 mm is adequate to properly capture the involved physical phenomena. In addition, we notice negligible differences in liquid tip predictions. Also vapor penetration trends are quite close to each other, with the k-g model matching the WALE in the initial transient state and the Smagorinsky in the final stage of the injection. These results validate the reliability of k-g model when mode II of our proposed approach is selected. To further investigate on the results, we show in Figure 6 the instantaneous mass fraction and velocity fields obtained for the k-g model, for the time instant t=1.5 ms, corresponding to the end of injection. In Figure 6, the Lagrangian particles of liquid are also shown, in order to provide a qualitative representation of the liquid penetration and liquid jet shape. Both particles diameters and velocity field are normalized to their maximum values, respectively. The flow structures seems to be consistent and the fields are described in details. Also, values of mass fraction are in line with those from other similar works available in literature [6, 7]. Further, we show in Figure 8 the instantaneous viscosity ratio distribution, at time t=1.5 ms after the start of injection. Figure 8 compares the results from the three turbulent models considered. Interestingly, the k-g and WALE viscosity fields are fairly similar, with the former exhibiting a smoother spatial distribution as typically expected for LES closures based on sub-grid transport equations [1]. Predictions from the standard Smagorinsky model are somewhat

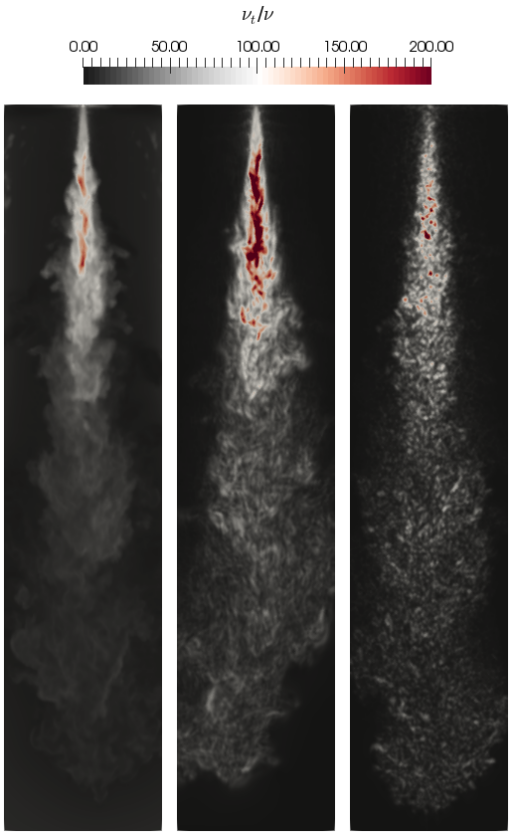

Figure 8: Turbulent viscosity ratio for LES on mesh *m2*. From left to right: k-g (with a_τ = 0.8), Smagorinsky, WALE.

overdiffusive compared to the others, which is again an expected behavior for this simple viscosity-based LES formulation [1].

As for mode I, we investigate on the effects of the turbulent kinetic energy initialization for the k-g model in mode II. Similarly to URANS simulations, we vary the value of the uniform initial field of k from 0.0735 m^2/s^2 up to 7.35 m^2/s^2. Simulations are carried out on mesh *m2*, and the analysis is depicted in Figure 9. Results are in line with those from URANS case. Liquid penetration is not affected by the initial choice of the value of k. However, the vapor penetration results to be slightly overestimated when relatively high values of k are set.

Finally, we present in Figure 10 results, in terms of liquid and vapor penetration, for LES performed via k-g and WALE models on mesh *m3*, which minimum size is 0.0625 mm. Prediction of liquid penetration on mesh *m3* appears to be significantly overestimated. Simulations from both the considered models, however, are in strict agreement to each other. From this result, we infer that, for the present case and with the specific choice of numerical setup, a mesh resolution of 0.0625 may not be suitable to accurately capture the main features of the spray, since it may violate the principles regulating the Eulerian-Lagrangian approach. On the other hand, we notice that the vapor penetration trend obtained from both k-g and WALE model is in line with experimental data. In particular, a mesh resolution of 0.0625 seems to lead, with respect to the coarser mesh *m2*, to an improvement of the vapor penetration slope, starting from about 0.3 ms up to the end of injection. This is particularly true for the k-g model. The mismatch in the slope prediction with experimental results during the initial transient state may be due to the inaccurate estimation of the liquid phase.

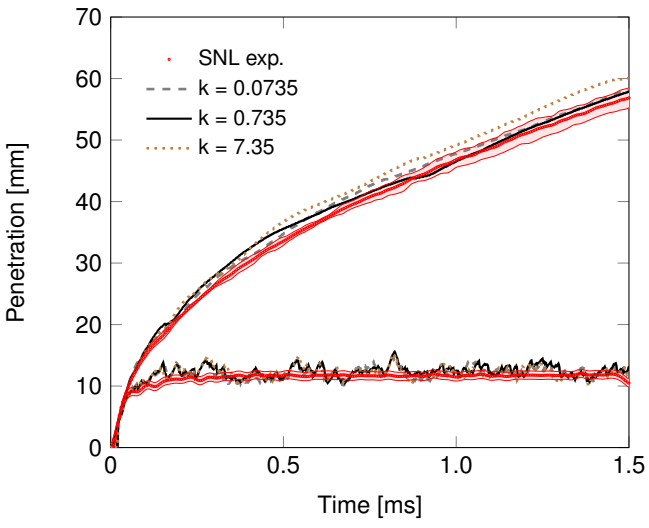

Figure 9: Effect of turbulence kinetic energy initialization for LES k-g model (with a_τ = 0.8) on liquid and vapor penetration. Simulations are performed on mesh *m2* (minimum size: 0.125 mm). Results are compared with experimental data of SNL [21]. The filled area corresponds to the experimental standard deviation.

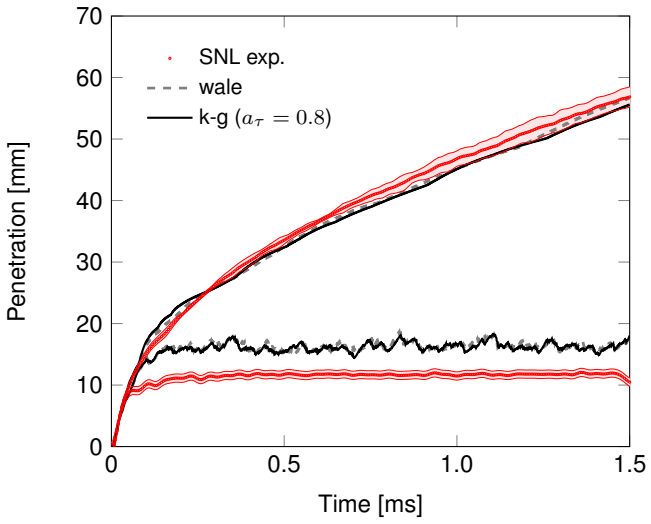

Figure 10: Effects of LES turbulence model on liquid and vapor penetration. Simulations are performed on mesh *m3* (minimum size: 0.0625 mm). Results are compared with experimental data of SNL [21]. The filled area corresponds to the experimental standard deviation.

DES simulations analysis (mode III)

In this Section, we study the behavior of the proposed model when operating in mode III, namely when a seamless DES is employed. To this aim, we perform numerical simulations on mesh *m2*. Also, the numerical setup and initial conditions are the same as for LES simulations on the same mesh. Model constant a_τ is set to 0.8. In Figure 11, results in terms of liquid and vapor penetrations are shown for three different cases corresponding to different values of the initial turbulent kinetic energy uniform field.

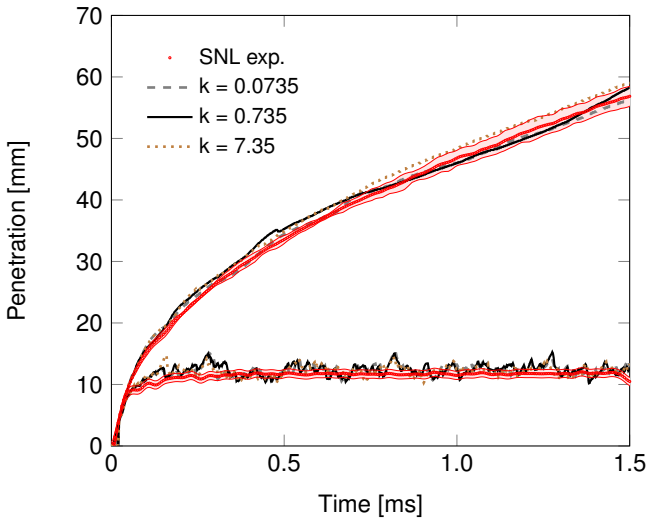

Figure 11: Effect of turbulence kinetic energy initialization for DES k-g model (with a_τ = 0.8) on liquid and vapor penetration. Results are compared with experimental data of SNL [21]. The filled area corresponds to the experimental standard deviation.

Satisfactory results are obtained, especially for low values of k. For these cases, predictions of both liquid and vapor penetration approach closely the experimental data. When the initial uniform field of turbulent kinetic energy is set to higher values, such as k = 7.35 m^2/s^2, the vapor tip results slightly overestimated. Overall, we notice that mode III exhibits a similar behavior to pure-LES simulations. In order to better understand this aspect and investigate on the features of the proposed model in mode III operating condition, we analyze the instantaneous fields of the parameter F_{DES}. For a more comprehensive understanding, we present in Figure 12 a visualization of the inverse of F_{DES} in the closest region to the injector hole. The instantaneous fields depicted in Figure 12 refer to three subsequent time instants, namely: t=0.03 ms, t=0.12 ms and t=0.21 ms. We recall that a value of $1/F_{DES}$ equal to 1 indicates pure-URANS operating condition, while values lower than 1 correspond to pure-LES mode. Figure 12 reveals interesting information about the present hybrid strategy for spray simulation. At the very beginning of the simulation the model operates as mode I, namely pure-URANS, almost over all the region of spray development (t=0.03 ms). This is expected since, during the first time instants after the start of injection, the flow experiences the highest velocity gradients and, as a consequence, mesh resolution in this region may be not sufficient to adequately resolve the spray dynamics with a LES approach. The behavior of DES changes during the subsequent time-steps. The model seems to switch from mode I to II everywhere in the spray region, with the exception of relatively small areas in the closest proximity of the injector, where higher velocity gradients still occur. Eventually, almost the whole developed spray region is handled by the DES model as a pure-LES. This further confirms the similar results obtained via the present hybrid approach to those from LES. These preliminary results indicate that, for the particular case under study, the DES strategy does not bring significant beneficial effects in terms of accuracy on the numerical solution or computational cost. In fact, we may infer that, for the present spray, the typical mesh resolution required to properly capture the liquid-gas interactions within the Lagrangian-Eulerian framework is generally lower than the URANS modeled turbulence length scale. For this reason, the pure-LES mode seems to be the preferred choice during DES operating conditions, over almost all the spray region.

Fuel mass fraction and velocity profiles

In this Section, we present a direct comparison among numerical results as obtained via the three modes, in terms of fuel mass fraction and velocity profiles, and with available experimental data. The case analyzed refer to the k-g closure model with constant a_τ equal to 0.8 and uniform initial turbulence kinetic energy field equal to 0.735 m^2/s^2, with URANS simulation being performed on mesh *m1* while both LES and DES simulations being performed on mesh *m2*.

Instantaneous axial velocity profiles are compared with those from experimental measurements of IFPEN [21]. To be consistent, we extend our simulations up to 1.6 ms. In Figures 13, 14 and 15, the instantaneous axial velocity along centerline and the ensemble-averaged instantaneous

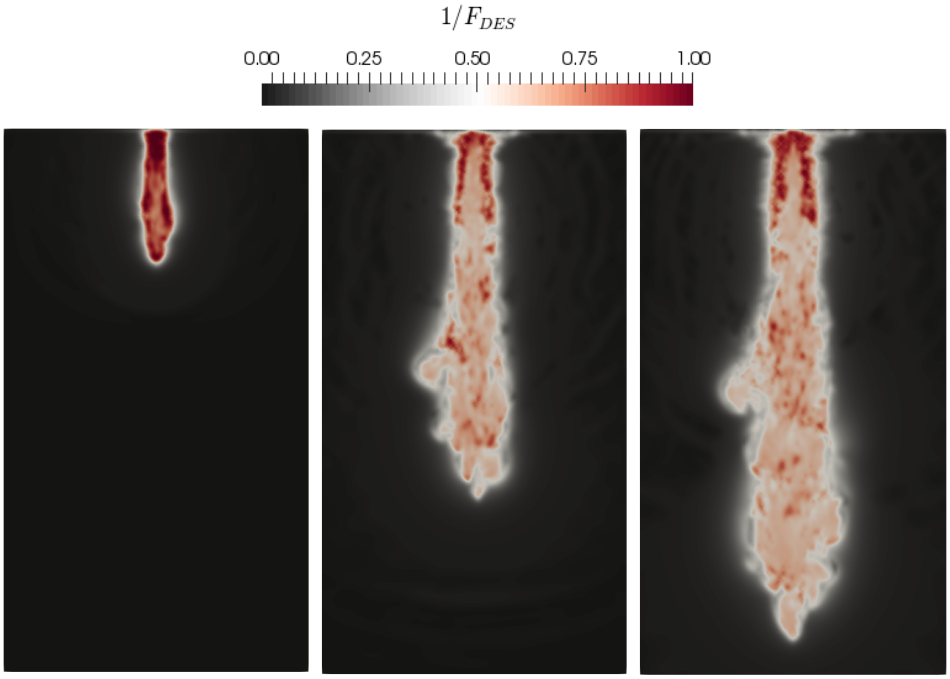

Figure 12: Snapshots of function $1/F_{DES}$ at (from left to the right): t = 0.03 ms, t = 0.12 ms, and t = 0.21 ms after the start of injection, for DES with k-g closure model (a_τ = 0.8) on mesh *m2*.

axial velocity at two different radial sections are presented. In particular, velocity radial profiles are obtained by performing spatial averaging in the azimuthal direction over 40 sample sections. Both numerical results and experimental data refer to conditions at the end of injection. Overall, simulation results from all of the three modes exhibit qualitatively similar trends. In particular, all of the numerical models predict velocity profiles within the experimental accuracy.

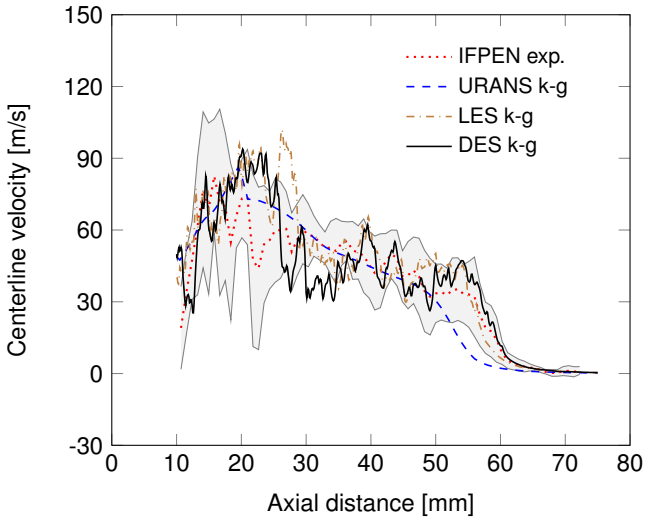

Figure 13: Instantaneous axial velocity profile along centerline at 1.6 ms after the start of injection as predicted by modes I, II and III, in comparison with experimental data from IFPEN [21] at the same time instant. The filled area corresponds to the experimental standard deviation.

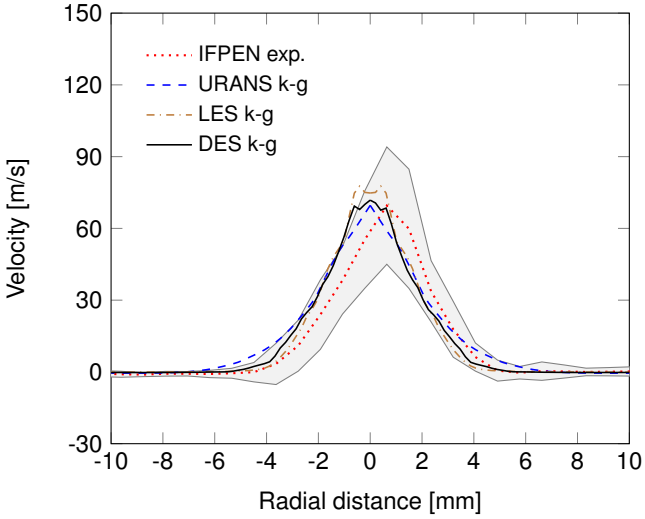

Figure 14: Instantaneous axial velocity profile along a radial section at 25 mm from the injector at 1.6 ms after the start of injection. Predictions from modes I, II and III are compared with experimental data from IFPEN [21] at the same time instant. Spatial averaging in the azimuthal direction is performed to simulations results. The filled area corresponds to the experimental standard deviation.

As expected, we observe no significant differences between LES and DES simulation results. This is in line with the findings discussed on previous Section. We emphasize that experimental data show a slightly off-axis profile. This is not the case for our numerical results which are, by construction, axis-symmetric.

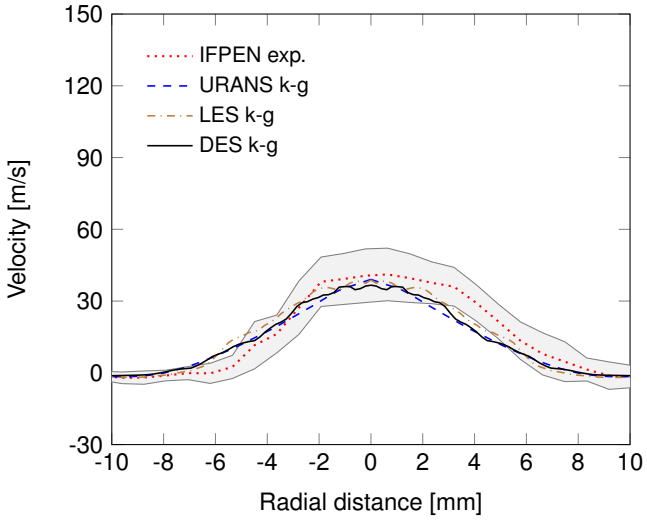

Figure 15: Instantaneous axial velocity profile along a radial section at 45 mm from the injector at 1.6 ms after the start of injection. Predictions from modes I, II and III are compared with experimental data from IFPEN [21] at the same time instant. Spatial averaging in the azimuthal direction is performed to simulations results. The filled area corresponds to the experimental standard deviation.

Next, we analyze the mixture fraction (which is equivalent to the fuel mass fraction, since the system is inert) along the centerline and at two different radial sections. In this case, the available experimental data are those of Pickett et al. [50], which are obtained via Rayleigh-scatter measurements. The ensemble-averaged experimental results refer to steady-state conditions. Therefore, in order to be consistent and compare our numerical results with experimental data, we perform a novel set of simulations by imposing an injection duration of 6.0 ms. The new ROI used in our simulations is shown in Figure 16, and the corresponding total injected mass is equal to 15.12 mg.

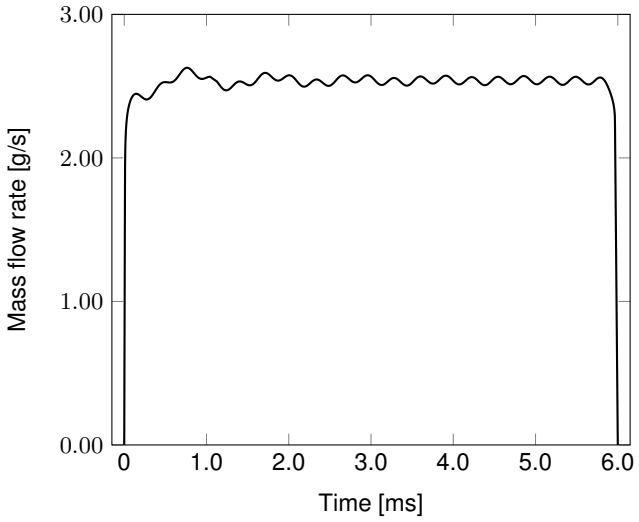

Figure 16: Rate of injection used as inflow condition.

All of the other simulations parameters are the same of those used in the previous cases presented in this work. To ensure that the jet is steady-state and that the initial transient of the jet head penetration do not affect the computation, we perform a time-averaging between 1.5 ms and 2.5 ms by collecting statistics at each time-step.

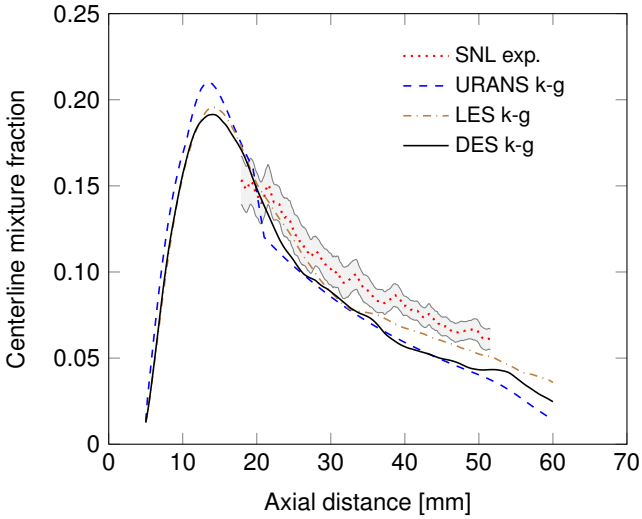

Figure 17: Mean mass fraction along centerline as predicted by modes I, II and III, in comparison with steady-state experimental data from Pickett et al. [50]. Spatial averaging in the azimuthal direction and time averaging from 1.5 to 2.5 ms are performed to simulation results. The filled area corresponds to the experimental measurement uncertainty with 95% confidence interval.

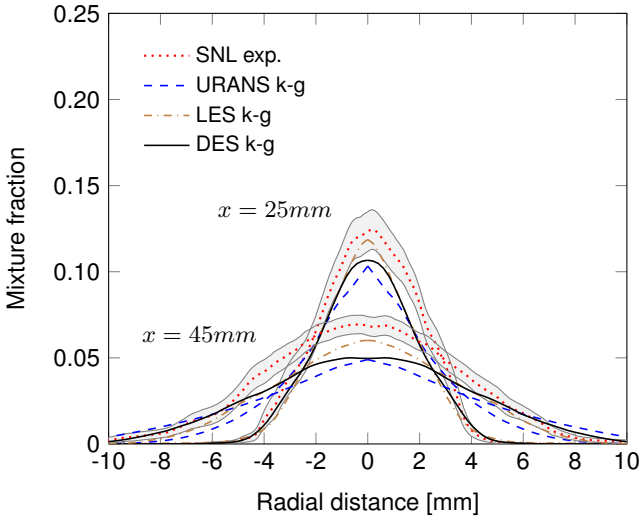

Figure 18: Mean mass fraction radial profiles as predicted by modes I, II and III, at 25 mm and 45 mm from the injector, in comparison with steady-state experimental data from Pickett et al. [50]. Spatial averaging in the azimuthal direction and time averaging from 1.5 to 2.5 ms are performed to simulation results. The filled area corresponds to the experimental measurement uncertainty with 95% confidence interval.

In Figures 17 and 18, we report the ensemble-averaged mean profiles of mass fraction along the centerline and at two radial sections, which are 25 mm and 45 mm distant to the inlet, respectively, as predicted by modes I, II and III, in comparison with experiments. All of the three modes seem to slightly underestimate the experimental trends. This is, however, in line with other numerical simulation results presented in the second ECN workshop [42]. In addition, we notice that our numerical results are in agreement with each other. In particular, DES and LES simulations provide more accurate radial profiles with respect to those obtained by URANS, as expected. These findings further confirm that, for the present case under study, the hybrid methodology provide accurate results which are aligned with those from a LES approach.

Numerical simulations presented in this work were run in parallel on a Dell PowerEdge M620 workstation, using 20 cores which features are: Intel(R) Xeon(R) CPU E5-2680 v2, 2.80GHz, RAM 128 GB. As far as the k-g turbulence model is concerned, URANS simulation on mesh *m1* required an overall execution time of roughly 2 hours to complete 1.5 ms of injection. Execution times for LES and DES simulations on mesh *m2*, for the same case, took about 14 and 13 hours, respectively. The computational cost of the last two modes is therefore comparable. This is due to the fact that, as discussed before, the DES approach mainly behaves as a pure-LES, especially during the subsequent stages after the initial transient.

Effect of Stochastic Turbulence Dispersion

In this Section, we investigate on the effects of the STD and we present results for analysis with modes II (LES) and III (DES) with k-g closure model and a_τ = 0.8. To this aim, we perform simulations on mesh *m2*, employing the same numerical setup of those used for the analogous cases previously described.

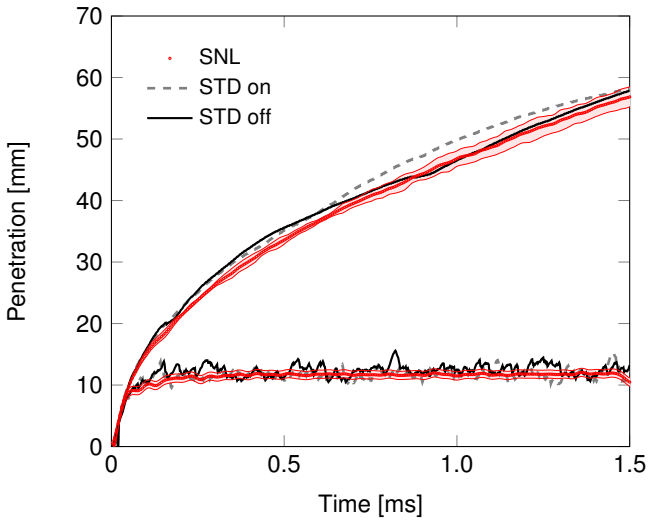

Figure 19: LES with k-g closure model (a_τ = 0.8) on mesh *m2*: effects of Stochastic Turbulent Dispersion (STD) on liquid and vapor penetration. The filled area corresponds to the experimental standard deviation.

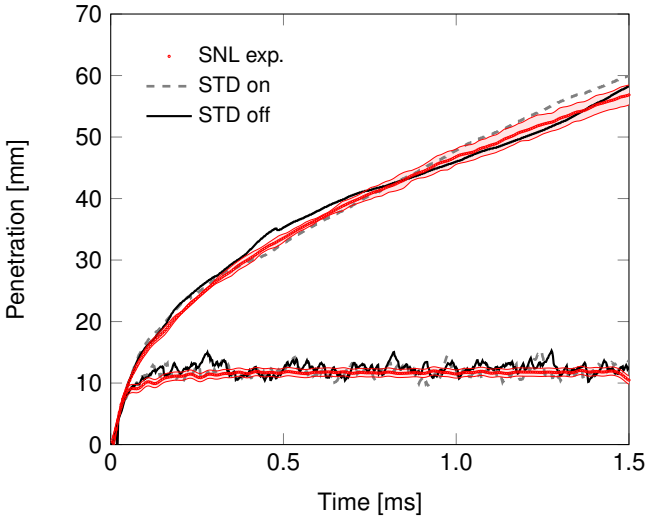

Figure 20: DES with k-g closure model (a_τ = 0.8) on mesh *m2*: effects of Stochastic Turbulent Dispersion (STD) on liquid and vapor penetration. The filled area corresponds to the experimental standard deviation.

Figures 19 and 20 show our numerical findings from k-g model simulations in comparison with experimental data. Differences between cases with and without modeling of STD are not significant in either LES and DES operating conditions. In particular, liquid penetration does not seem to be affected by the STD, while the vapor penetration tips are slightly over predicted when STD is active. However, both approaches seem to reasonably capture the experimental trend.

From this preliminary analysis we observe that STD modeling plays a similar role in LES and DES approaches. This was expected, given the highlighted similar behavior between the two modes. However, further consolidation is needed before a judgment can be made on the impact of STD on both LES and DES. In particular, future studies should be aimed to I) improve the STD model and II) extend the analysis to more realistic study-cases. In particular, focus should be posed on the method of choosing the turbulence correlation time. This is indeed the most influential parameter of STD modeling.

Conclusions

The present study was aimed to provide useful insights on the coupling of LPT spray modeling with hybrid URANS/LES turbulence formulations. More specifically, our goal was to: I) investigate the consistency of the pure-URANS and pure-LES modes of the proposed zonal hybrid approach; II) evaluate the usage of seamless DES for spray simulation. In addition to that, a preliminary study was conducted to understand the impact of STD modeling in both LES and DES operating modes. In order to accomplish to these tasks, we took into consideration the canonical case of standard "`Spray A`" configuration. Such a relatively easy-to-handle case allows a direct analysis of numerical effects

given by the turbulence modeling, while avoiding prone error factors which are related to complex geometries.

After a tuning procedure of the spray sub-models, which was conducted by means of URANS approach, we tested the numerical behavior of the k-g closure model for either URANS and LES operating conditions. Results are satisfactory, since they evidence the reliability of k-g model to handle the spray simulation numerical problem. Our findings are in good agreement with experimental data available from literature. Moreover, we obtained a good agreement between results from the k-g model and those related to other more commonly used approach, such as RNG k-ε for URANS and Smagorinsky and WALE for LES.

Further, we investigated on DES, by making a comparative analysis with previous findings from LES and experimental data. Apparently, for the particular case-study, the use of an hybrid dynamic strategy seems to not lead to significant advantages, in terms of accuracy, on the prediction of the main spray features and involved physical phenomena. This can be partially justified by analyzing the instantaneous behavior of the F_{DES} function, which dynamically regulates the switch between the two operating modes, namely URANS and LES. From F_{DES} fields, we notice that DES operates basically as a pure-LES, since the refinement level of the computational mesh seems to be dictated by the strict Lagrangian-Eulerian coupling requirements.

Finally, we considered the STD on both LES and DES approaches. Our results indicate no significant influence by the STD modeling. However, an in-depth analysis is in order to better understand the impact of STD related factors, such as the choice of the turbulence correlation time. This can be the subject of future works, together with the development of more accurate models for STD.

Acknowledgments

All the reported numerical simulations were performed on the *Zeus* HPC facility, at the University of Naples "Parthenope". The *Zeus* facilty has been realized through the Italian Government Grant PAC01_00119 *MITO - Informazioni Multimediali per Oggetti Territoriali*, with Prof. Elio Jannelli as the Scientific Responsible.

References

1. C. J. Rutland. Large-Eddy Simulations for internal combustion engines - a review. *International Journal of Engine Research*, 12(5):421–451, 2011.

2. S. Fontanesi, A. D'Adamo, and C. J. Rutland. Large-Eddy Simulation analysis of spark configuration effect on cycle-to-cycle variability of combustion and knock. *International Journal of Engine Research*, 16(3):403–418, 2015.

3. K. Truffin, C. Angelberger, S. Richard, and C. Pera. Using Large-Eddy Simulation and multivariate analysis to understand the sources of combustion cyclic variability in a spark-ignition engine. *Combustion and Flame*, 162:4371–4390, 2015.

4. N. Bharadwaj, C. J. Rutland, and S. Chang. Large eddy simulation modelling of spray-induced turbulence effects. *International Journal of Engine Research*, 10(2):97–119, 2009.

5. V. Vuorinen, H. Hillamo, O. Kaario, M. Nuutinen, M. Larmi, and L. Fuchs. Effect of droplet size and atomization on spray formation: A priori study using large-eddy simulation. *Flow, Turbulence and Combustion*, 86(3):533–561, 2011.

6. A. Wehrfritz, V. Vuorinen, O. Kaario, and M. Larmi. Large eddy simulation of high-velocity fuel sprays: Studying mesh resolution and breakup model effects for spray A. *Atomization and Sprays*, 23(5):419–442, 2013.

7. M. Jangi, R. Solsjo, B. Johansson, and X.-S. Bai. On large eddy simulation of diesel spray for internal combustion engines. *International Journal of Heat and Fluid Flow*, 53:68 – 80, 2015.

8. C.-W. Tsang, C.-W. Kuo, M. Trujillo, and C. Rutland. Evaluation and validation of large-eddy simulation subgrid spray dispersion models using high-fidelity volume-of-fluid simulation data and engine combustion network experimental data. *International Journal of Engine Research*, in press, 2018.

9. C. Hasse, V. Sohm, and B. Durst. Detached eddy simulation of cyclic large scale fluctuations in a simplified engine setup. *International Journal of Heat and Fluid Flow*, 30:32–43, 2009.

10. S. Buhl, F. Dietzsch, C. Buhl, and C. Hasse. Comparative study of turbulence models for scale-resolving simulations of internal combustion engine flows. *Computers & Fluids*, 156:66–80, 2017.

11. S. Buhl, D. Hain, F. Hartmann, and C. Hasse. A comparative study of intake and exhaust port modeling strategies for scale-resolving engine simulations. *International Journal of Engine Research*, 19(3):282–292, 2018.

12. F. Piscaglia, A. Montorfano, and A. Onorati. A scale adaptive filtering technique for turbulence modeling of unsteady flows in ic engines. *SAE Int. J. Engines*, 8(2):426–436, 2015.

13. Y. Wu, A. Montorfano, F. Piscaglia, and A. Onorati. A study of the organized in-cylinder motion by a dynamic adaptive scale-resolving turbulence model. *Flow, Turbulence and Combustion*, 100(3):797–827, Dec 2018.

14. C. Hasse, V. Sohm, and B. Durst. Numerical investigation of cyclic variations in gasoline engines using a hybrid URANS/LES modeling approach. *Computers & Fluids*, 39:25–48, 2010.

15. V. K. Krastev, G. Bella, and G. Campitelli. Some developments in DES modeling for engine flow simulation. *SAE Paper 2015-24-2414.*, 2015.

16. V. K. Krastev and G. Bella. A zonal turbulence modeling approach for ICE flow simulation. *SAE Int. J. Engines*, 9(3):1425–1436, 2016.

17. V. K. Krastev, L. Silvestri, G. Falcucci, and G. Bella. A zonal-LES study of steady and reciprocating engine-like flows using a modified two-equation DES turbulence model. *SAE Paper 2017-24-0030.*, 2017.

18. V. K. Krastev, L. Silvestri, and G. Falcucci. A modified version of the RNG k-ε turbulence model for the scale-resolving simulation of internal combustion engines. *Energies*, 10:2116, 2017.

19. F. Piscaglia, A. Montorfano, and A. Onorati. Development of a Non-Reflecting Boundary Condition for Multidimensional Nonlinear Duct Acoustic Computation. *Journal of Sound and Vibration*, 332(4):922–935, 2013.

20. V. K. Krastev, G. Di Ilio, G. Falcucci, and G. Bella. Notes on the hybrid URANS/LES turbulence modeling for internal combustion engines simulation. *Energy Procedia*, 148:1098–1104, 2018.

21. https://ecn.sandia.gov/.

22. P. R. Spalart. Detached-Eddy Simulation. *Annu. Rev. Fluid Mech.*, 41:181–202, 2009.

23. A. Travin, M. L. Shur, M. Strelets, and P. R. Spalart. Physical and numerical upgrades in the Detached-Eddy Simulation of complex turbulent flows. In R. Friedrich and W. Rodi, editors, *Advances in LES of Complex Flows*, pages 239–254. Kluwer Academic Publishers, Netherlands, 2002.

24. G. Kalitzin, A. R. B. Gould, and J. J. Benton. Application of two-equation turbulence models in aircraft design. *AIAA Paper 96-0327*, 1996.

25. D. C. Wilcox. Reassessment of the scale-determining equation for advanced turbulence models. *AIAA Journal*, 26(11):1311–1320, 1988.

26. G. Bella and V. K. Krastev. On the RANS modeling of turbulent airflow over a simplified car model. In *ASME-JSME-KSME 2011 Joint Fluids Engineering Conference: Volume 1, Symposia Parts A, B, C, and D*, pages 871–883. ASME, 2011.

27. V. K. Krastev and G. Bella. On the steady and unsteady turbulence modeling in ground vehicle aerodynamic design and optimization. *SAE Paper 2011-24-0163*, 2011.

28. P. A. Durbin. On the k-ε stagnation point anomaly. *International Journal of Heat and Fluid Flow*, 17:89–90, 1996.

29. P. A. Durbin. Limiters and wall treatments in applied turbulence modeling. *Fluid Dynamics Research*, 41(1):012203, 2009.

30. P. Sagaut, S. Deck, and M. Terracol. *Multiscale and multiresolution approaches in turbulence – LES, DES and Hybrid RANS/LES Methods: Applications and Guidelines*. Imperial College Press, 2013.

31. S. Deck. Zonal-Detached-Eddy Simulation of the flow around a high-lift configuration. *AIAA Journal*, 43(11):2372–2384, 2005.

32. S. Deck. Recent improvements in the Zonal Detached Eddy Simulation (ZDES) formulation. *Theor. Comput. Fluid Dyn.*, 26(6):523–550, 2012.

33. S. Deck, F. Gand, V. Brunet, and S. Ben Khelil. High-fidelity simulations of unsteady civil aircraft aerodynamics: stakes and perspectives. Application of zonal detached eddy simulation. *Phil. Trans. R. Soc. A*, 372, 2014.

34. S. H. El Tahry. k-ε equation for compressible reciprocating engine flows. *J. Energy*, 7(4):345–353, 1983.

35. T.-H. Shih, W. W. Liou, A. Shabbir, Z. Yang, and J. Zhu. A new k-ϵ eddy viscosity model for high reynolds number turbulent flows. *Computers & Fluids*, 24(3):227 – 238, 1995.

36. Z. Han and R. D. Reitz. Turbulence modeling of internal combustion engines using RNG k-ε models. *Combust. Sci. and Tech.*, 106:267–295, 1995.

37. J. Smagorinsky. General circulation experiments with the primitive equations: I. The basic experiment. *Mon. Weather Rev.*, 91(3):99–164, 1963.

38. F. Nicoud and F. Ducros. Subgrid-scale stress modelling based on the square of the velocity gradient tensor. *Flow, Turbulence and Combustion*, 62(3):183–200, 1999.

39. P.J. O'Rourke. Statistical properties and numerical implementation of a model for droplet dispersion in a turbulent gas. *Jounral of Computational Physics*, 83:345–360, 1989.

40. A.A. Amsden, P.J. O'Rourke, and T.D. Butler. KIVA-II: A Computer Program for Chemically Reactive Flows with Sprays. *Los Alamos National Laboratory*, LA-11560-MS, 1989.

41. R.D. Reitz. Modeling Atomization Processes in High-pressure Vaporizing Sprays. *Atomization and Spray Technology*, 3:309–337, 1987.

42. https://ecn.sandia.gov/ecn-workshop/.

43. J.C. Beale and R.D. Reitz. Modeling spray atomization with the Kelvin-Helmhotz / Rayleigh-Taylor hybrid model. *Atomization and Sprays*, 9:623–650, 1999.

44. M.A. Patterson and R.D. Reitz. Modeling the Effects of Fuel Spray Characteristics on Diesel Engine Combustion and Emission. *SAE Technical Paper 980131*, 1998.

45. J. Xin, L. Ricart, and R.D. Reitz. Computer Modeling of Diesel Spray Atomization and Combustion. *Combustion Science and Technology*, 137:171–176, 1998.

46. D.B. Spalding. The combustion of liquid fuels. *Symposium (International) on Combustion*, 4:847864, 1953.

47. B. Zuo, A.M. Gomes, and Rutland C.J. Studies of Superheated Fuel Spray Structures and Vaporization in GDI Engines. *International Journal of Engine Research*, 1:321–336, 2000.

48. https://www.cmt.upv.es/ECN03.aspx.

49. https://cfd.direct/openfoam/user-guide/.

50. L.M. Pickett, J. Manin, C.L. Genzale, D.L. Siebers, M.P.B. Musculus, and C.A. Idicheria. Relationship between diesele fuel spray vapor penetration/dispersion and local fuel mixture fraction. *SAE Int. J. Engines*, 4(1):764–799, 2011.